Ultrafast Melting of Carbon Induced by Intense Proton Beams

A. Pelka,[1] G. Gregori,[2,3] D. O. Gericke,[4] J. Vorberger,[4] S. H. Glenzer,[5] M. M. Günther,[1] K. Harres,[1] R. Heathcote,[3] A. L. Kritcher,[5] N. L. Kugland,[5,6] B. Li,[3] M. Makita,[7] J. Mithen,[2] D. Neely,[3] C. Niemann,[5,6] A. Otten,[1] D. Riley,[7] G. Schaumann,[1,3] M. Schollmeier,[1,8] An. Tauschwitz,[9] and M. Roth[1]

[1]*Technische Universität Darmstadt, IKP, Schlossgartenstraße 9, 64289 Darmstadt, Germany*
[2]*Department of Physics, University of Oxford, Parks Road, Oxford OX1 3PU, United Kingdom*
[3]*Central Laser Facility, Rutherford Appleton Laboratory, Chilton, Didcot OX11 0QX, United Kingdom*
[4]*Centre for Fusion, Space and Astrophysics, Department of Physics, University of Warwick, Coventry CV4 7AL, United Kingdom*
[5]*Lawrence Livermore National Laboratory, 7000 East Avenue, Livermore, California 94550, USA*
[6]*Physics Department, University of California—Los Angeles, Los Angeles, California 94550, USA*
[7]*Department of Physics and Astronomy, Queen's University Belfast, University Road, Belfast BT7 1NN, United Kingdom*
[8]*Sandia National Laboratories, Albuquerque, New Mexico 87185, USA*
[9]*Goethe-Universität Frankfurt am Main, Max-von-Laue-Str. 1, 60438 Frankfurt am Main, Germany*

(Received 5 July 2010; revised manuscript received 5 October 2010; published 23 December 2010)

Laser-produced proton beams have been used to achieve ultrafast volumetric heating of carbon samples at solid density. The isochoric melting of carbon was probed by a scattering of x rays from a secondary laser-produced plasma. From the scattering signal, we have deduced the fraction of the material that was melted by the inhomogeneous heating. The results are compared to different theoretical approaches for the equation of state which suggests modifications from standard models.

DOI: 10.1103/PhysRevLett.105.265701 PACS numbers: 64.70.dj, 52.50.Jm, 52.59.−f, 52.72.+v

Despite the fact that carbon is one of the most common elements on Earth, its phase diagram including the melt line is poorly understood [1]. In fact, the liquid state cannot be reached at ambient pressure as carbon directly sublimes into the gas phase. Yet liquid carbon may exist at the high pressures in the interior of giant planets such as Uranus and Neptune, where it can contribute to the magnetic moment. Furthermore it may appear on white dwarfs and in carbon-rich extra solar planets [2,3]. Thus, accurate equation of state (EOS) data are needed to develop realistic models for planetary formation [4] as well as to describe the structure of giant planets [5,6]. Our present knowledge of the carbon phase diagram is, however, almost entirely based on theory and simulations [7–9] as experimental data, e.g., on shock-compressed diamond [10,11] or low density carbon [12], are sparse. In this work, we investigate the EOS and melting of graphite at solid densities. The thermodynamics near melting is then inferred from a combination of measured energy inputs and the molten volume in inhomogeneously heated, macroscopic (≈ 6 μg) samples.

The creation of fluid carbon requires a rapid energy input. Ion beams are a unique tool for that task as they deposit their energy deep in the target [13]. Today's conventional, accelerator-based ion beams do not match both the high particle number and the short pulse length required to create fluid carbon without noticeable expansion. Ultrashort proton bursts generated by high-intensity laser beams [14–16] offer a feasible alternative.

The characterization of dense matter created by proton beams is a major challenge as the samples are opaque to visible light. Indeed, first investigations of proton-heated matter relied on measuring the surface properties applying emission spectroscopy [17], velocity interferometry [18], or chirped-pulse interferometry [19]. The bulk properties are then inferred from hydrodynamic modeling. Here, we abandon this method and measure the bulk properties of carbon directly by x-ray scattering [20–22]. The use of ultrafast x-ray sources [21,23] allows us to study the sample before the hydrodynamic expansion sets in.

Figure 1 shows the schematic layout of the experiment conducted at the Vulcan Laser Facility at the Rutherford Appleton Laboratory (UK). This laser system provides two high-energy, short-pulse beams. One 1054 nm beam with 60 J in 1 ps was focused by a $f/3$ parabola to a 10 μm spot on a 20 μm thin gold foil. This led to a focused intensity of $\sim 10^{20}$ W/cm^2 creating an intense proton beam. The second laser with 180 J in 18 ps at the same wavelength was used to drive a titanium He-α source. This produced an intense x-ray burst at 4.75 keV photon energy and with a similar duration [21,23]. The x rays scattered off the carbon sample and were detected by a spectrometer under 90° from the incident radiation. For recording the scattering signal, we used a curved high-reflectivity, highly oriented pyrolytic graphite (HOPG) crystal in von Hamos geometry together with a Fuji maximum sensitivity image plate detector and a 125 μm beryllium filter that blocks the visible light [24]. During the experiment the x-ray source was directly monitored for each laser shot using a second spectrometer with a flat HOPG crystal. Extensive shielding ensured that only scattering from the marked region was detected.

Because of the large angular spread, a fraction of the proton beam did not pass through the target [see Fig. 2].

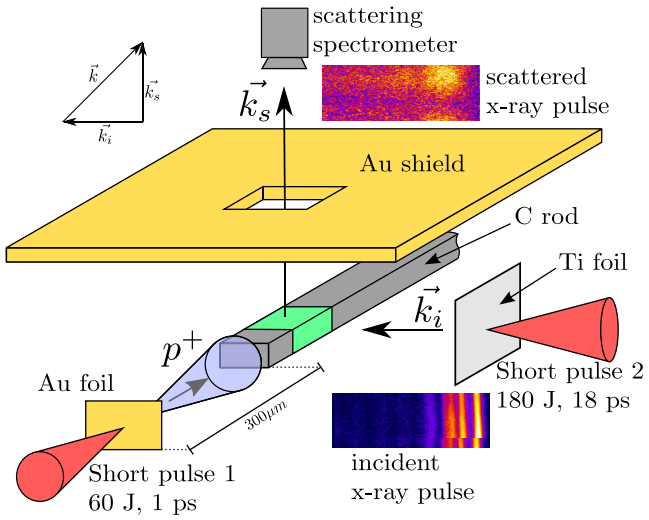

FIG. 1 (color online). Schematic layout: a polycrystalline graphite rod (125 μm $\times$ 300 μm $\times$ 3 mm) is heated by the protons produced by the laser coming from the lower left. The second laser hits a titanium foil to produce an intense x-ray pulse which is scattered off the green region of the sample and detected by a spectrometer above the target at 90°. The gold shielding blocks the line of sight from the laser spots to the scattering spectrometer as well as the front and back regions of the carbon rod. The RCF proton detector and the source radiation spectrometer are not shown.

This part was detected by a stack of radiochromic films (RCF). The absolutely calibrated RCF give a two-dimensional distribution of the laser-generated protons and their energy distribution relating the penetration depth into the RCF stack to the proton energy. The full angular distribution including energy-dependent opening angles and particle numbers was measured by taking shots without a scattering target. This method allows us to determine the proton spectrum for each shot leaving only the in-beam distribution as an uncertainty source. In this experiment, we find particle numbers in the range of 4×10^{11} with maximum energies of 17 MeV, in agreement with previous work [16].

The measurements of the proton beam fully determine the heating source. Using the known energy loss data for protons in cold graphite [25], the energy deposition profile inside the target can be calculated. For this purpose, we used the hydrodynamic code MULTI2D modified to model the energy deposition [26]. Utilizing tabulated EOS, the code also generates temperature profiles. From them, the region that underwent melting, that is where $T \gtrsim T_m = 0.39$ eV, was obtained from the measured proton beam spectrum. Figure 3 shows results based on two different EOS models: the standard SESAME library [27] (table 7832) and an EOS that was calculated by *ab initio* simulations [28,29]. The results from density functional theory molecular dynamics (DFT-MD) predict a significantly larger coexistence region related to the latent heat of melting which generates the plateau region in Fig. 3.

The x-ray scattering geometry corresponds to a change in the photon wave number of $k = (4\pi E_0/hc)\sin(\theta_s/2) = (3.4 \pm 0.2)$ Å^{-1}, where $E_0 = 4.75$ keV and θ_s is the scattering angle. The spread originates from the finite size of the HOPG crystal in the nondispersive direction. In the analysis we apply x-ray diffraction where the scattering signal is frequency integrated and thus only k dependent.

For our experiment, we must consider scattering from systems containing solids, fluids, or both phases. Thus, the intensity of the scattered radiation is given by

$$I_{sc} = CI_0[V_s S_s^{\mathrm{tot}}(k) + V_l S_l^{\mathrm{tot}}(k)], \quad (1)$$

where the index labels solid (s) and liquid (l) properties. The factor C includes the Thomson cross section, the

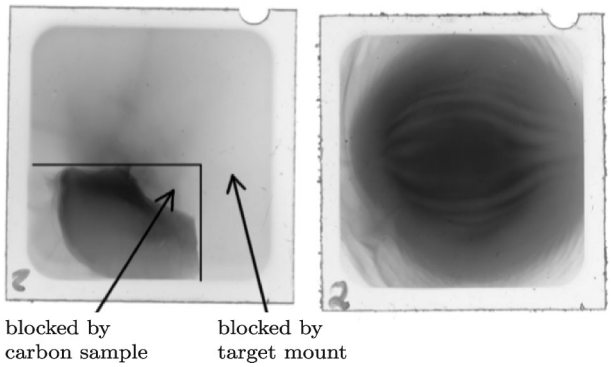

FIG. 2. Samples of RCF used to monitor the proton beam. A picture taken with the full target (left) shows the regions that are blocked by the target mount and the carbon sample. The right panel shows the whole proton beam taken without a target. The lines originate from a structure on the backside of the foil. They were used to determine the source size.

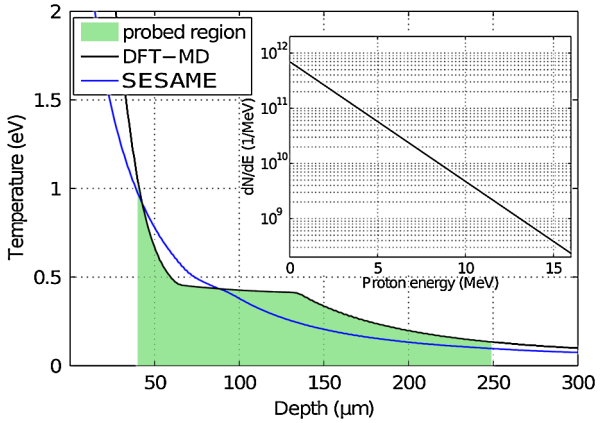

FIG. 3 (color online). Temperature profile along the axis together with the energy spectrum of the protons used for this simulation. The total energy deposited in the carbon sample is 180 mJ. The grey (green) area marks the region probed by x-ray scattering.

polarization factor, the geometry of the sample, and the attenuation of x rays in the material. I_0 is the incident intensity, $V_{s,l}$ are the volumes probed, and $S^{\mathrm{tot}}_{s,l}(k)$ is the total (static) electron structure factor for solids or fluids, respectively. The latter fully determines the measured differences between solids and fluids.

The structure factor can be divided in contributions due to quasielastic scattering, inelastic scattering, and incoherent scatter [20]. In contrast to recent investigations of warm dense matter [20–22], the free electron part and contributions due to the screening cloud are here negligible as the ionization degree is very low. In this limit, the static, frequency-integrated structure factors for solids (s) and liquids (l) can be written as [30,31]

$$S^{\mathrm{tot}}_{s,l} = |f(k)|^2 S_{ii}(k) + Z_C[1 - |f(k)|^2/Z_C^2]. \qquad (2)$$

Here, $f(k = 3.4\ \text{Å}^{-1}) = 2.82$ is the atomic form factor, $S_{ii}(k)$ is the static ion-ion structure factor, and $Z_C = 6$ is the nuclear charge.

For solids, the scattering signal is dominated by the incoherent (second) part in Eq. (2). The quasielastic contribution is very small as under 90° scattering the Bragg-condition is not fulfilled for any orientation of microcrystals in the amorphous samples; small contributions arise from volume elements scattering at $k = 3.5\ \text{Å}^{-1}$, corresponding to diffraction from the (012) planes. Since for scattering from unheated solid graphite C and V_s are known, the total structure factor for solid carbon was determined by an absolute measurement of the source and scattered intensities I_0 and I_{sc}.

In the liquid, the strength of the incoherent scattering is unchanged. On the other hand, elastic scattering is strongly increased as the ionic structure factor for liquids has its first and strongest peak near the wave number we probe. Moreover, the Hansen-Verlet criterion states that the height of this first peak has a value of 2.85 at the melting temperature [32] and the atomic form factor is given by the atomic physics [30]. Thus, the strength of the elastic feature in the fluid near the melt line is fully determined by basic principles and is independent of theoretical structure models.

The energy of the protons is not sufficient to melt the whole sample. The inhomogeneous heating typically creates a fluid region near the proton source whereas deeper parts are still solid. The total electron structure factors are quite different for fluid carbon and graphite ($S_{ii} \simeq 0$ for cold graphite, whereas $S_{ii} \simeq 2.85$ for molten carbon). Thus, the scattering intensity described by Eq. (1) is a function of the fraction of material melted. The strong increase of the measured scattering intensity with energy deposited as seen in Fig. 4(a) must thus be attributed to melting. The horizontal error bars account for both uncertainties in the proton beam spectrum and thickness of the sample.

The phase-dependence of the scattering strength can be used to infer the portion of carbon that has undergone

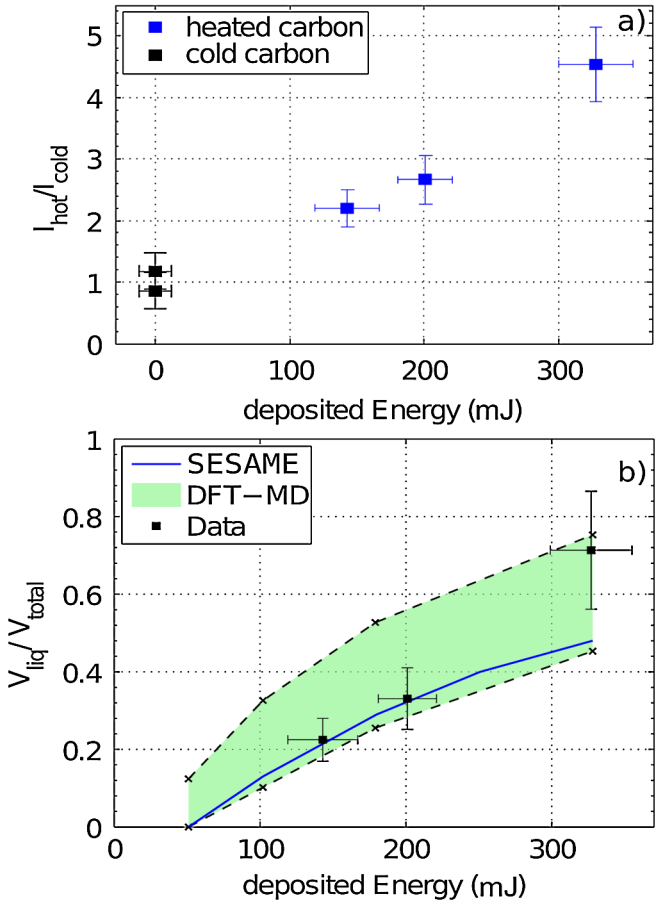

FIG. 4 (color online). (a) Ratio of the measured scattering intensity of heated and unheated graphite versus the energy that was deposited in the probed volume. (b) Fraction of molten carbon in the probed volume versus energy input. Experimental data are compared to theoretical modeling based on the SESAME EOS tables for carbon and the DFT-MD model.

melting. Combining the total intensity (1) with the structure factor applied to fluids and solids (2) yields a relation between the measured scattering intensity (normalized to that of cold matter) and the liquid fraction of the sample

$$\frac{V_l}{V_{\mathrm{tot}}} = \left(\frac{I_{\mathrm{hot}}}{I_{\mathrm{cold}}} - 1\right)\left(\frac{S^{\mathrm{tot}}_l}{S^{\mathrm{tot}}_s} - 1\right)^{-1}. \qquad (3)$$

Here, the ionic structure factors were averaged with respect to all occurring wave numbers k. Still, the main part of the scattering comes from $k = 3.4\ \text{Å}^{-1}$ and coherent scattering from the solid is small. We also assume the liquid to be very close to the melt line, as most of the energy is needed for the phase transition. Therefore, the results presented in Fig. 4(b) are a lower bound for the fluid fraction as hotter fluids will scatter less at the probed wave numbers.

Figure 4(b) shows the measured ratio V_l/V_{tot} together with the molten fraction extracted from the heating profiles in the simulations. As no significant expansion occurs

during the 18 ps of the x-ray probe, our data are taken at solid densities of $\rho = 2.25$ g/cm^3. For lower doses, the experimental data agree well with the modeling based on either EOS model applied. The uncertainty related to the large solid-fluid coexistence region in the DFT-MD EOS is reflected in the green band whereas the lower limit assumes characteristics similar to fluid, and the upper limit to solid carbon [33]. The good agreement of the SESAME EOS with the data underlines that it is accurate for the well-tested cases of heated solids. Indeed, previous work [19] showed a good match between experiments and modeling based on SESAME.

At higher energy inputs when more of the material becomes fluid, we find increasing deviations between the measured and the modeled data if the SESAME EOS is used. As our data give a lower bound to the fluid fraction, we can state that SESAME EOS overestimates the heat capacity for graphite close to melting. The EOS from DFT-MD on the other hand matches the measured fluid fractions as it accounts for more latent heat. It predicts a pressure of ≈ 7.5 GPa in the fluid phase in agreement with molecular dynamics calculations [8]. Our measurements indicate that *ab initio* simulations may be a more accurate tool to fully describe the phase transition in carbon at the highest deposited energy.

The present data explore new territory indeed, and this work represents an important step towards the realization of laboratory analogues of extreme extraterrestrial planetary environments. The correct modeling of the liquid content at high pressures in carbon-rich planets and white dwarfs has far-reaching implications, for example, on the predicted magnetic fields. Current models often assume that the magnetic field is generated through a dynamo process such that the radial field scales as $B \sim L^{-2} \sim V_l^{-2/3}$ [34], where L is the length scale of the rotation zone. Hence, the observed differences in the molten volume may result in a decrease of the predicted radial magnetic field strength up to 50%.

We thank the CLF staff at RAL for their assistance. The work of A. P., M. M. G., K. H., A. O., M. S., and M. R. was supported by the BMBF, support codes 06DA9043I, 06DA9044I, and 05KS7SJ1. The work of G. G., and B. L. was partially supported by the STFC. The work of J. M. was supported by the John Fell Fund. Support from EPSRC grants is acknowledged by G. G. (EP/G007187/1), D. G., J. V. (EP/D062837), and D. R., M. M. (EP/C001869/1). The work of N. L. K., A. L. K., and S. H. G. was supported by LDRD Grant No. 08-ERI-002 and was performed under the auspices of the U.S. Department of Energy by the Lawrence Livermore National Laboratory under Contract No. DE-AC52-07NA27344. We also acknowledge support from the LLNL Lawrence Scholar Program. Sandia is operated by Lockheed Martin Corp. for the U.S. DOE (Contract No. DE-AC04-94AL85000).

[1] A. A. Correa, S. A. Bonev, and G. Galli, Proc. Natl. Acad. Sci. U.S.A. **103**, 1204 (2006).
[2] P. Dufour *et al.*, Nature (London) **450**, 522 (2007).
[3] S. Stanley and J. Bloxham, Nature (London) **428**, 151 (2004).
[4] H. C. Connolly, Jr. and S. G. Love, Science **280**, 62 (1998).
[5] W. B. Hubbard *et al.*, Science **253**, 648 (1991).
[6] B. Militzer *et al.*, Astrophys. J. Lett. **688**, L45 (2008).
[7] M. P. Grumbach and R. M. Martin, Phys. Rev. B **54**, 15730 (1996).
[8] J. N. Glosli and F. H. Ree, Phys. Rev. Lett. **82**, 4659 (1999).
[9] X.-F. Wang, S. Scandolo, and R. Car, Phys. Rev. Lett. **95**, 185701 (2005).
[10] M. D. Knudson *et al.*, Science **322**, 1822 (2008).
[11] J. H. Eggert *et al.*, Nature Phys.**6**, 40 (2010).
[12] A. Cavalleri *et al.*, Europhys. Lett. **57**, 281 (2002).
[13] D. H. H. Hoffmann *et al.*, Phys. Plasmas **9**, 3651 (2002).
[14] E. L. Clark *et al.*, Phys. Rev. Lett. **84**, 670 (2000).
[15] R. A. Snavely *et al.*, Phys. Rev. Lett. **85**, 2945 (2000).
[16] M. Roth *et al.*, Phys. Rev. ST Accel. Beams **5**, 061301 (2002).
[17] P. K. Patel *et al.*, Phys. Rev. Lett. **91**, 125004 (2003).
[18] G. M. Dyer *et al.*, Phys. Rev. Lett. **101**, 015002 (2008).
[19] A. Mancic *et al.*, High Energy Density Phys. **6**, 21 (2010).
[20] S. H. Glenzer and R. Redmer, Rev. Mod. Phys. **81**, 1625 (2009).
[21] A. L. Kritcher *et al.*, Science **322**, 69 (2008).
[22] E. Garcia Saiz *et al.*, Nature Phys. **4**, 940 (2008).
[23] B. Barbrel *et al.*, Phys. Rev. Lett. **102**, 165004 (2009).
[24] I. J. Paterson *et al.*, Meas. Sci. Technol. **19**, 095301 (2008).
[25] J. F. Ziegler, Nucl. Instrum. Methods Phys. Res., Sect. B **219-220**, 1027 (2004).
[26] A. Tauschwitz *et al.*, High Energy Density Phys. **2**, 16 (2006).
[27] S. P. Lyon and J. D. Johnson, LANL Report No. LA-UR-92-3407, 1992.
[28] K. Wünsch, J. Vorberger, and D. O. Gericke, Phys. Rev. E **79**, 010201(R) (2009).
[29] See supplementary material at http://link.aps.org/supplemental/10.1103/PhysRevLett.105.265701.
[30] G. Gregori *et al.*, Phys. Plasmas **11**, 2754 (2004).
[31] R. James, *The Optical Principles of the Diffraction of X-rays* (Ox Bow Press, London, 1962).
[32] J.-P. Hansen and L. Verlet, Phys. Rev. **184**, 151 (1969).
[33] Two-phase DFT-MD simulations are computationally very expensive. Here, we consider either fluids or solids in ρ-T space and then we computed heating profiles through this phase space.
[34] R. L. Kirk and D. J Stevenson, Astrophys. J. **316**, 836 (1987).